Climatology of marine shallow-cloud-top radiative cooling

Youtong Zheng[1], Yannian Zhu[2], Daniel Rosenfeld[3], and Zhanqing Li[4]

[1]University of Maryland, College Park
[2]School of Atmospheric Sciences, Nanjing University
[3]Hebrew University of Jerusalem
[4]UMD/ESSIC

November 23, 2022

Abstract

A one-year's worth of global (except poleward of 65 º N/S) marine shallow single-layer cloud-top radiative cooling (CTRC) is derived from a radiative transfer model with inputs from the satellite cloud retrievals and reanalysis sounding. The mean cloud-top radiative flux divergence is 61 Wm^{-2}, decomposed into the longwave and shortwave components of 73 and -11 W m^{-2}, respectively. The CTRC is largely a reflection of free-atmospheric specific humidity distribution: a dry atmosphere enhances CTRC by reducing downward thermal radiation. Consequently, the cooling minimizes in the "wet" tropics and maximizes in the "dry" eastern subtropics. Poleward of 30 º N/S, the CTRC decreases slightly due to the colder clouds that emit less effectively. The CTRC exhibits distinctive seasonal cycles with stronger cooling in the winter and has amplitudes of order 10~20 Wm^{-2} in stratocumulus-rich regions. The datasets were used to train a machine-learning model that substantially speeds up the retrieval.

Climatology of marine shallow-cloud-top radiative cooling

Youtong Zheng[1,2], Yannian Zhu[3], Daniel Rosenfeld[3,4], and Zhanqing Li[1]

Affiliations:
[1]Earth System Science Interdisciplinary Center, University of Maryland, College Park, Maryland, 20742, USA.
[2]GFDL/AOS program, Princeton University, Princeton, New Jersey
[3]Nanjing University, Nanjing, China
[4]Herew University of Jerusalem, Jerusalem, Israel

Main points:

- A one-year's worth of global marine shallow single-layer cloud-top radiative cooling (CTRC) is derived from satellite and reanalysis data.
- Spatial and seasonal variations of CTRC are largely reflections of changes in free-tropospheric humidity.
- A neural network model for the CTRC was trained, which substantially speeds up the retrieval while maintaining good accuracy.

Abstract

A one-year's worth of global (except poleward of 65 º N/S) marine shallow single-layer cloud-top radiative cooling (CTRC) is derived from a radiative transfer model with inputs from the satellite cloud retrievals and reanalysis sounding. The mean cloud-top radiative flux divergence is 61 Wm^{-2}, decomposed into the longwave and shortwave components of 73 and -11 W m^{-2}, respectively. The CTRC is largely a reflection of free-atmospheric specific humidity distribution: a dry atmosphere enhances CTRC by reducing downward thermal radiation. Consequently, the cooling minimizes in the "wet" tropics and maximizes in the "dry" eastern subtropics. Poleward of 30 º N/S, the CTRC decreases slightly due to the colder clouds that emit less effectively. The CTRC exhibits distinctive seasonal cycles with stronger cooling in the winter and has amplitudes of order 10~20 Wm^{-2} in stratocumulus-rich regions. The datasets were used to train a machine-learning model that substantially speeds up the retrieval.

Plain Language Summary

Marine low-lying clouds cool the Earth by reflecting incoming sunlight, thus crucially important for the Earth's climate. Marine low clouds cool by emitting thermal radiation. The cooling is known as cloud-top radiative cooling (CTRC). A change in CTRC can influence the properties of marine clouds via many avenues, ranging from altering the vertical motions of the clouds to changing the clouds' ability to reflect sunlight. Despite the importance of CTRC to the climate system, its climatological characteristics, namely how it varies with space and time, remain unknown. This work fills this knowledge gap. We generate the product of the CTRC over the global ocean using a novel satellite methodology developed in our previous work. Analyses of the data show that the spatial and temporal distributions of the CTRC are largely reflections of the atmospheric humidity: the drier the atmosphere, the stronger the cooling. As a result, the CTRC maximizes in the wet tropics and minimizes in the dry eastern subtropical ocean such as the west of California. We also use the CTRC data to train a machine-learning algorithm that can substantially speed up the calculation of CTRC.

1. Introduction

Marine shallow clouds (MSC) are crucially important to the Earth's climate because they affect both energy and water cycles. MSC cloudiness is dominated by stratocumulus decks sustained by the convection driven by cloud-top radiative cooling (CTRC). An increase in CTRC destabilizes the stratocumulus-topped boundary layer, driving more intense convective circulation that substantially alter the cloud and radiative properties via many avenues (Lilly, 1968; Deardorff, 1976; Nicholls, 1984; Austin et al., 1995; Bretherton and Wyant, 1997; Stevens, 2002; Caldwell et al., 2005; Bretherton et al., 2007; Zheng et al., 2016, 2018; Zhou and Bretherton, 2019). These influences make the CTRC a crucial player in understanding the low cloud feedback, a major source of uncertainty for climate projections (Bony and Dufresne, 2005). For example, as the planet warms, the CTRC will weaken due to the enhanced down-welling thermal radiation in a more opaque atmosphere. The reduced CTRC, via weakening the boundary layer convection, thins the stratocumulus decks, leading to positive low cloud feedback. Representations of CTRC in the global climate models (GCMs) are poor because the cooling typically concentrates near the top several tens of meters of the cloud layer, which the GCMs cannot resolve. An improved representation of CTRC in a modern higher-order turbulence closure scheme in GCMs (Larson et al., 2012) can markedly improve the GCM simulations of low clouds (Guo et al., 2019).

Despite the fundamental importance of CTRC, its observations have been scarce. Typical approaches are direct observations of radiative fluxes from aircraft (Bretherton et al., 2010b) or tethered balloon (Slingo et al., 1982) and indirect calculations with a radiative transfer model (RTM) with inputs from field campaign measurements (Nicholls and Leighton, 1986; Wood, 2005; Ghate et al., 2014; Zheng et al., 2016). The ensuing CTRC data are inherently highly limited in spatial and temporal coverage. Active satellite sensors have been used to estimate the radiative fluxes in the cloudy atmosphere using a radiative transfer model (L'Ecuyer et al., 2008; Haynes et al., 2013), but the vertical resolution is too coarse (240 m) to resolve the CTRC that takes place chiefly near the upper several tens of meters in MSC. A systematic analysis of the CTRC climatology over the global ocean is still lacking.

This study aims to fill the knowledge gap of CTRC climatology. This work builds upon our previous work by Zheng et al. (2019) who proposed a new remote sensing approach for retrieving the CTRC with passive satellite data. This new methodology calculates the CTRC using an RTM with inputs from satellite-derived cloud properties and reanalysis sounding corrected by satellite-retrieved cloud-top temperature. Here we used the method to generate a full year of MSC CTRC product from the Moderate Resolution Imaging Spectroradiometer (MODIS) onboard the National Aeronautics and Space Administration Aqua and Terra satellites. The data were used in two ways: studying the CTRC climatology and training a machine learning model to speed up the retrieval.

The paper is organized as follows: Section 2 introduces satellite data and the algorithm of CTRC retrieval. Section 3 provides a theoretical background of the environmental dependence of CTRC, paving the ground for the subsequent analyses. Section 4 analyzes the climatology of CTRC in terms of spatial and temporal variabilities. Section 5 shows the machine learning of CTRC and its evaluations, followed by the conclusion in Section 6.

2. Data and Methodology

2.1. Data

Cloud properties are obtained from the MODIS Terra/Aqua Level-1 (MxD06) and Level-2 (MxD06_L2) cloud product collection 6.1 (Platnick et al., 2015) over the global ocean in 2014. Each MODIS swath was divided into multiple 110 by 110 km scenes (~ 1° by 1° at the equator). The criteria for scene selection are the same as our previous works (Rosenfeld et al., 2019; Cao et al., 2021). Scenes with single-layer liquid water clouds with cloud geometrical thickness thinner than 800 m were selected. In each scene, the retrieved cloud optical depth, cloud droplet effective radius, and cloud top temperature are averaged over cloudy pixels. Scenes poleward of 65 ° N or S are excluded to avoid the known problems of cloud retrievals for high solar zenith angle (Grosvenor and Wood, 2014). A total of ~ 6 million valid scenes were collected.

Vertical profiles of temperature and humidity are obtained from the National Centers for Environmental Prediction reanalysis data (Kalnay et al., 1996). The sea surface temperature (T_s) data are from the National Oceanic and Atmospheric Administration (Reynolds et al., 2007). The reanalysis and T_s data are interpolated into the geological center and time of each satellite scene.

2.2. Retrieval algorithm

We provide a high-level introduction of this algorithm to elucidate the fundamental concepts (Zheng et al., 2019). The retrieval relies on an RTM (see text S1) with inputs from satellite-retrieved cloud parameters in combination with the reanalysis sounding. The key merit of this algorithm is the revision of the original reanalysis profiles. It is well known that reanalysis data fail to capture the sharp inversion layer topping MSC. This causes large errors in the simulated radiative fluxes across the cloud top that are particularly sensitive to temperature inversion. We tackled this challenge by revising the reanalysis sounding in a physically coherent way. We use the satellite-retrieved cloud-top temperature to reconstruct the inversion-layer sounding by assuming a 100% relative humidity in the cloud layer (see Zheng et al., 2019 for detail).

With inputs from the revised sounding and satellite-retrieved cloud parameters, the radiative transfer model outputs the vertical profiles of radiative fluxes. We quantify the CTRC using the divergence of net radiative flux across the cloud top, denoted as ΔF. The upper boundary for ΔF is 100 m above the cloud top and the lower boundary is the height of the grid in the cloud layer where the radiative cooling shifts to radiative warming as one goes down to the cloud base (there is typically radiative warming layer near the cloud base). The ΔF has longwave (LW) and shortwave (SW) components (ΔF_{LW} and ΔF_{SW}).

Because Terra/Aqua satellites have fixed overpasses time of approximately 1030 and 1330 h local solar time, the simulated SW fluxes are biased toward the local time of observations when the incoming solar insolation is substantially larger than the daily means. To mitigate such diurnal bias, we follow L'Ecuyer et al. (2008) to correct the instantaneous SW flux by multiplying it by a correcting factor defined as the ratio of the average top-of-atmosphere insolation for the scene's latitude and Julian day to the instantaneous top-of-atmosphere insolation. Figure S1 shows the probability density function (PDF) of the instantaneous ΔF_{SW} (red) and corrected daily mean ΔF_{SW} (green). The daily mean ΔF_{SW} is considerably smaller and more narrowly distributed than the instantaneous ΔF_{SW}, consistent with expectation. In the remainder of the manuscript, the ΔF_{SW} refers to the daily mean ΔF_{SW} unless otherwise noted.

Note that the ΔF represents cooling averaged over cloudy pixels of a satellite scene and there is no contribution from the cloud-free area. In other words, the cloudiness does not directly influence the ΔF. This is important to keep in mind because some studies refer to the CTRC as the average of all pixels, both clear and cloudy (Bretherton et al., 2010a; Vial et al., 2016). Such an all-sky CTRC is not our focus although it will be discussed in Section 4.3.

Aerosols are not included in the calculations because of the lack of aerosol vertical information from passive sensors. We consider it an insignificant issue, motivated by previous research showing the limited radiative role of aerosols compared with the influence of atmospheric thermodynamics (Haynes et al., 2013; Henderson et al., 2013).

3. Conceptual background: what determines the CTRC?

To assist with interpreting the climatology analysis, we briefly discuss what drives the changes in ΔF_{SW} and ΔF_{LW} using simple illustrative formulas. The ΔF_{LW} for a single-layer cloud can be approximated as:

$$\Delta F_{LW} \approx \varepsilon_c \sigma T_c^4 - \varepsilon_a \sigma T_a^4, \quad (1)$$

where ε, σ, and T are the emissivity, the Stefan-Boltzmann constant, and emission temperature, respectively. The subscripts "c" and "a" stand for the cloud and the above-cloud atmosphere, respectively. The ΔF_{LW} is typically positive, meaning a divergence of radiative flux and thus a cooling. Given the small variability of T_c/T_s (Figure S2) due to low altitudes of MSC, Eq. (1) can be simplified to:

$$\Delta F_{LW} \approx \sigma T_s^4 \times (\varepsilon_c - \varepsilon_a \frac{T_a^4}{T_s^4}), \quad (2)$$

For SW, we use the Schwarzschild equation to derive an illustrative formula for ΔF_{SW}:

$$\Delta F_{SW} \approx S \times e^{-\tau_a} \times (1 - e^{-\tau_c}), \quad (3)$$

where S stands for the incoming SW radiative flux at the top of the atmosphere, which is negative. τ is a bulk measure of an atmospheric layer's ability to absorb SW energy (i.e. SW optical depth). In a clear atmosphere, its primary contribution is primarily from the water vapor whereas in a cloudy layer both cloud droplets and water vapor contribute (Li and Moreau, 1996). Note that the equation is a simplified formula for an illustrative purpose only.

Equations 2 and 3 show several important CTRC-controlling factors. The first is the optical thickness of the free atmosphere. For LW, an optically thicker free atmosphere enhances the emissivity (ε_a), thereby increasing the downward radiative flux. This decreases the cooling. In the atmosphere, water vapor is the most important absorber so a more humid atmosphere favors weaker cloud-top LW cooling. For SW, a humid free atmosphere absorbs more incoming solar radiation (a smaller $e^{-c\tau_a}$), leaving less energy for the cloud to absorb (Davies et al., 1984). So humid atmosphere weakens cloud absorption of SW radiation. This compensates for the reduced LW cooling.

The second CTRC-controlling factor is the cloud liquid water path (LWP). In the LW, the ε_c increases with the LWP (Pinnick et al., 1979) so that the LW cooling is larger for thicker clouds (Zheng et al., 2016; Zheng et al., 2019). The degree of dependence is large for thin clouds with LWP < 50 g m^{-3} and saturates afterward (Kazil et al., 2017). In the SW, the solar absorption also increases with the LWP (Stephens, 1978). A large LWP typically corresponds to a more humid layer, thereby enhancing the solar absorption due to the high concentration of water vapor. As a result, the ΔF_{SW} must increase with LWP. This, again, leads to a cancelation for the net CTRC. The cloud droplet effective radius also alters CTRC but its contribution is much smaller (Zheng et al., 2019).

Another two factors are the σT_s^4 and S. We discuss them together because they are highly correlated in nature. Climatologically speaking, more solar insolation corresponds to warmer sea surfaces to maintain radiative balance. This holds in both spatial (zonal-mean meridional distribution) and temporal (seasonal cycle) senses.

In summary, to the first order, the CTRC variation can be explained from four factors: the free-atmospheric humidity, LWP, σT_s^4 and S. The climatological co-variation of the last two factors can reduce the number of influential factors to three.

4. Result

The CTRC product shows that the ΔF, ΔF_{LW}, and ΔF_{SW} have means of 61 W m^{-2}, 73 W m^{-2}, and -11 W m^{-2}, respectively (Fig. S1). The ΔF PDF is similar to that of ΔF_{LW}, but with weaker cooling and less variability due to the compensation by ΔF_{SW}. Below we analyze the CTRC climatology in terms of spatial (Sect. 4.1) and temporal (Sect. 4.2) variations.

4.1. Annual mean

Figure 1 a~c show the annual-mean ΔF scaled by the σT_s^4 and its LW and SW components. The scaling temporarily frees us from considering the roles of T_s and, to a great extent, S. The σT_s^4-scaled ΔF, ΔF_{LW}, and ΔF_{SW} share a similar spatial pattern: a strong latitudinal dependence with the weakest cooling (or heating) in the tropics and the strongest in the extra-tropics, regional peaks in the eastern subtropics adjacent to the major continents, and hemispheric asymmetry with stronger cooling/heating in the Southern Hemisphere.

Such a spatial pattern can be well explained by the free atmospheric humidity. The specific humidity at 700 hPa (q_{700}) (Fig. 1d) highly resembles the σT_s^4-scaled CTRC variables in terms of the spatial pattern. This is consistent with the theoretical argument that drier free atmosphere enhances the cloud-top LW cooling by weakening the down-welling thermal radiation (Fig. 1b) and strengthens the cloud-top SW heating by increasing the exposure of clouds to solar insolation (Fig. 1c). The reduced SW heating compensates for the LW cooling, but because the magnitude of the ΔF_{SW} is considerably smaller than the ΔF_{LW}, the net effect, ΔF, largely follows the ΔF_{LW}.

The LWP contributes little. Over most regions, the climatological LWP is large enough (> 50 gm^{-3}) that the sensitivity of ΔF_{LW} to the LWP already saturates (Zheng et al., 2016; Kazil et al., 2017). The most illustrative example is the tropical eastern Pacific Ocean where there is a band of high LWP. The local LWP peak is caused by the strong convective activities that also moisten the free atmosphere, leading to large q_{700}. The two factors oppositely change the ΔF. The pattern of

$\Delta F/\sigma T_s^4$ and its components still follows the q_{700} whose influences dominate over the LWP. There are some footprints of LWP on the local variability of $\Delta F_{SW}/\sigma T_s^4$ such as the scattered blobs and bands of red colors in the southern part of the Southern Oceans, but the overall spatial pattern of the scaled $\Delta F/\sigma T_s^4$ is a reflection of the free-tropospheric humidity.

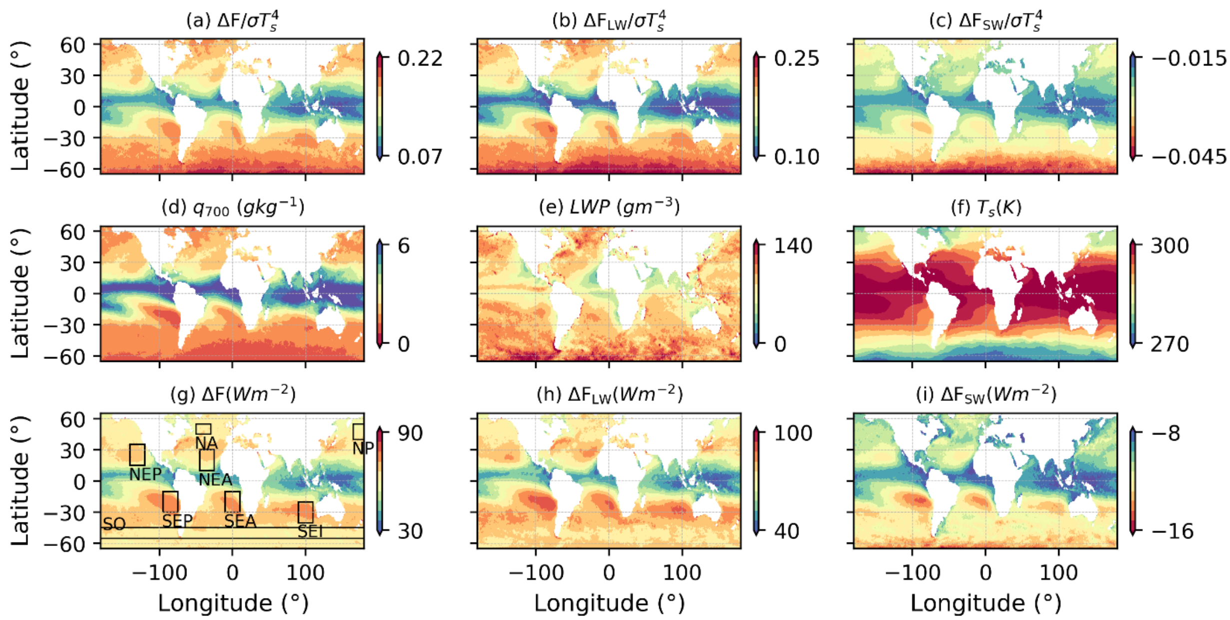

Figure 1: Global distribution of annually-averaged cloud-top radiative cooling scaled by σT_s^4 (a), its LW (b) and SW components (c), specific humidity at 700 hPa (d), liquid water path (e), sea surface temperature (f), and cloud-top radiative cooling (g) and its LW (h) and SW components (i). In (g), black rectangles mark regions with persistent low clouds and the locations are adopted from Klein and Hartmann (1993), with slight modifications of limiting regions within 55 ºN/S to avoid seasonal sampling bias.

Having known the ability of free-tropospheric humidity in explaining the $\Delta F/\sigma T_s^4$, we now look at the ΔF (bottom panel of Figure 1). The pattern is overall similar to the $\Delta F/\sigma T_s^4$ in the tropical regions where the variation of T_s is not large enough to alter the ΔF feature. The influence of σT_s^4 is most distinctive in the extratropical regions where the low solar zenith angle and the cold sea surface considerably weaken the SW heating and LW cooling, respectively, despite the bands of maximums in the southern flank of the Southern Ocean likely due to the large LWP. As a result, the peaks of ΔF no longer concentrate in the extratropical oceans where the q_{700} is lowest but locate in the eastern subtropical basins where both the dry free atmosphere and the moderate sea surface favor the strong LW cooling.

The roles of q_{700} and σT_s^4 can be more clearly seen from the zonal-mean meridional distributions (Fig. 2). The annual-mean scaled CTRC (Fig. 2b) monotonously increases with the latitude, consistent with the q_{700} variation (Fig. 2c). Without the scaling of σT_s^4, the CTRC starts to weaken poleward of ~30 º N or S (Fig. 2a) due to the cold temperature. This leads to local maximums of ΔF in ~ 30 º N or S where the downward branches of the Hadley circulation generate a very dry atmosphere and thus enhance LW cooling.

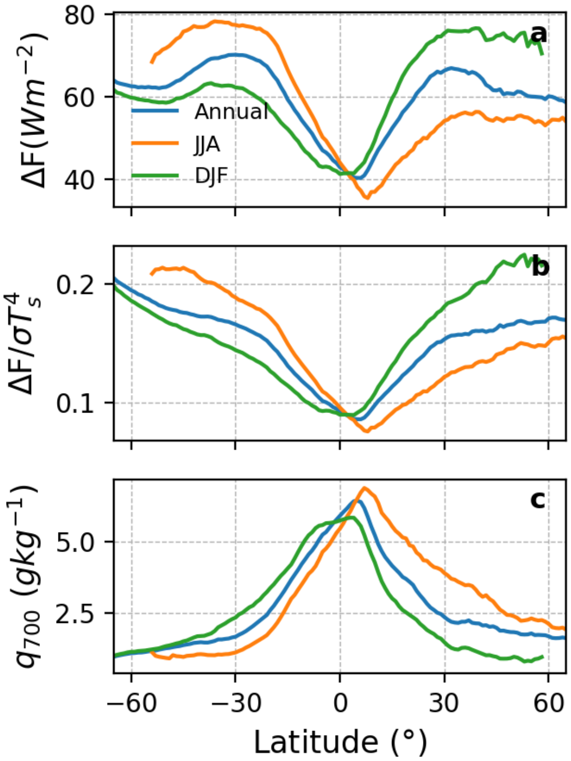

Figure 2: Zonal-mean meridional variations of cloud-top radiative cooling (a), cloud-top radiative cooling scaled by σT_s^4 (b), and specific humidity at 700 hPa (c) for the annual mean (blue) and boreal summer (orange) and winter months (green).

4.2. Seasonal cycle

The seasonal cycle manifests as the change in atmospheric temperature. The atmospheric temperature influences the ΔF both directly (via σT_s^4) and indirectly (via q_{700} under the constraint of Clausius-Clapeyron physics), with the former opposing the latter. The vapor effect dominates, suggested by Figure 2. The ΔF is stronger in the winter because of the low specific humidity (favoring the strong cooling) despite the lower temperature (not favoring strong cooling). The determinant control of atmospheric humidity is more clearly seen by the seasonally varying ΔF (and the scaled ΔF) being in phase with the q_{700} (Fig. 2c), both shifting with the seasonal movement of the solar insolation.

We further look at specific regions with frequent occurrence of stratocumulus decks: Northeast pacific (NEP), Northeast Atlantic (NEA), North Pacific (NP), North Atlantic (NA), Southeast Pacific (SEP), Southeast Atlantic (SEA), Southeast Indian Ocean (SEI), and Southern Ocean (SO). The locations of these regions are marked by rectangles in Figure 1g. Figure 3 shows the seasonal cycles of ΔF, along with the specific humidity profiles in boreal summer (June, July, and August) and winter (December, January, and February), for these regions. All regions show distinctive seasonable cycles with stronger cooling in the winter when the atmosphere is drier. The magnitudes are smallest over the subtropical Pacific oceans (NEP, 10 Wm^{-2}, and SEP, 11 Wm^{-2})

and largest over northern mid-latitudes (NP, 20 Wm^{-2}, and NA, 22 Wm^{-2}). There are two reasons for the larger amplitudes in the northern mid-latitudes. First, the atmospheric temperature and thus *q* experience more distinctive seasonal cycles in the mid-latitudes than the subtropics. Second, the response of LW cooling to the humidity of the overlying atmosphere is non-linear. The increase of the CTRC with the atmospheric desiccation is more rapid in a dry atmosphere than in a humid atmosphere (Zheng, 2019). The mid-latitudes are drier than the subtropics. Note that the cloud-top height is another influential factor for the CTRC because for a given humidity profile a higher cloud intrudes into a drier atmospheric layer, increasing the exposure of the cloud to the cold space, which enhances the cooling. In the northern mid-latitudes, cloud tops are higher in the summer due to the stronger convection propelled by warmer sea surface (Fig. 3d and e). This enhances the summertime CTRC, somewhat damping the humidity-driven seasonal cycle.

Interestingly, the SO experiences a markedly smaller degree of seasonal cycle (15 Wm^{-2}) than its counterparts in the northern hemisphere (NA and NP). The moisture profiles of SO (Fig. 3i) show only a slight increase in the moisture in the austral summer. This seems consistent with previous studies documenting a lack of seasonal cycle for SO MSC properties (Huang et al., 2012; Muhlbauer et al., 2014). Note that samples are selected for the single-layer MSC only. In mid-latitudes, such a cloud regime typically occurs in the colder section of mid-latitude cyclones, causing a sampling bias toward these regions. This sampling bias may be responsible for the lack of seasonal variation. To confirm this idea, needed is investigating the complex coupling between the low clouds, atmospheric thermodynamics, and synoptic dynamics, which is beyond the scope of this study.

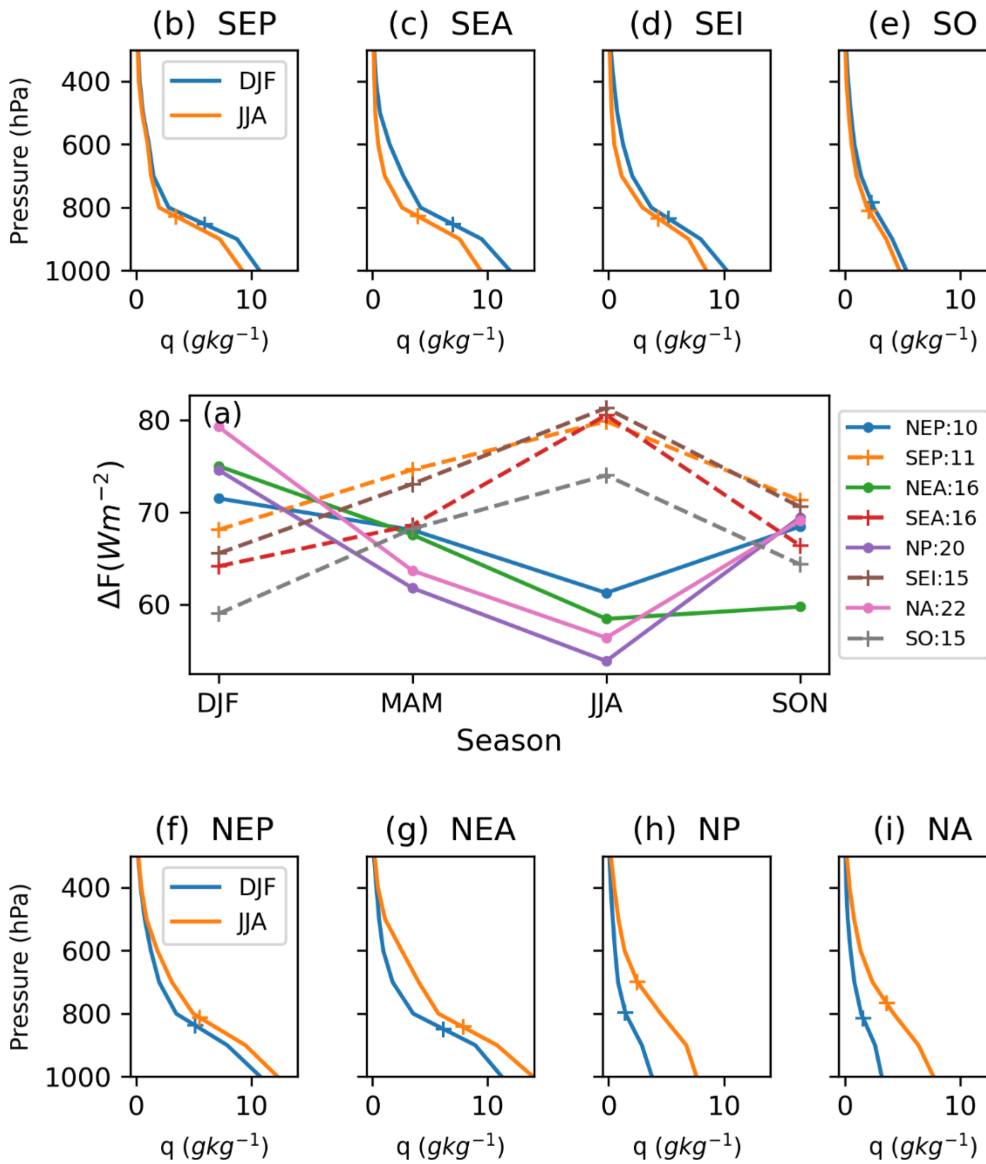

Figure 3: Seasonal cycle of cloud-top radiative cooling for selected regions marked in Fig. 1g (a). The numbers shown in the legend are the amplitudes of the seasonal cycle. (b)~(i) show the specific humidity profiles of the boreal summer and winter months for the eight selected regions. The plus symbols mark the cloud tops.

4.3. Discussion: relationship to stratocumulus cloudiness

The scaled ΔF spatial distribution closely resembles that of the cloudiness of marine stratocumulus (Fig. 4a in Wood 2012): the cloudiness peaks in the eastern subtropics and mid-latitudes, and has minimums in the tropics and western sides of the major ocean basins, and there is a hemispheric asymmetry with greater cloudiness in the southern hemisphere. One might take this resemblance for granted because the convective circulation in the stratocumulus is primarily driven by the CTRC. Without sufficiently strong CTRC, the stratocumulus decks cannot last long. Here we explain the resemblance from another perspective, with a focus on the environmental dependences of the two factors. Stratocumuli typically occur in subsiding atmospheres (Wood, 2012). On one hand, the subsidence helps maintain the shallowness of the cloud-topped boundary layer, sustaining the cloud-surface coupling that feeds moisture from the sea surface to the clouds. On the other hand, the subsiding portion of a region typically corresponds to the cold surface (the physics of thermally driven circulation). Cold water favors overcast stratocumuli in two ways. First, the more stable lower troposphere associated with the cold water helps sustain cloudiness via trapping water vapor within the boundary layer (Klein and Hartmann, 1993; Wood and Bretherton, 2006). Second, the weak surface fluxes associated with the cold water prevent the surface-heating-driven convection that breaks the stratocumulus decks (Wyant et al., 1997; Stevens et al., 1998). Both factors (subsidence and coldness) cause strong CTRC. The subsidence dries out the free atmosphere above the cloud top, enhancing CTRC. The cold temperature drops the free atmospheric specific humidity via Clausius-Clapeyron relationship, again strengthening the CTRC. In a nutshell, environments favoring the occurrence of overcast stratocumulus decks also favor strong CTRC.

The rough correspondence between CTRC and MSC cloudiness can be used to explain the spatial pattern of all-sky CTRC (Fig. S3), computed as the multiplication of the two. There is a substantial contrast between the eastern subtropics and the tropics. The all-sky CTRC in eastern subtropics and mid-latitudes remain as large as > 50 Wm^{-2} due to the large cloud coverage (annual mean of 40 ~ 60%) whereas tropical oceans have all-sky CTRC of only a few W m^{-2} largely caused by the small shallow cloud coverage.

5. Machine learning the CTRC

The major limitation of this CTRC retrieval algorithm is its reliance on running an RTM that is computationally expensive. To address this issue, we propose to use machine learning. Machine learning has been widely used in radiative transfer modeling (e.g. Krasnopolsky et al., 2010; Ukkonen et al., 2020). Among the machine learning algorithms, the artificial neural network (NN) is of particular interest because of its advantage of low computational cost: once it is trained, it is computationally efficient. This strength makes it suited to our needs.

The NN used in this study is based on the Python library Keras from TensorFlow (see Text S2 for detail). Table S1 lists the input and output variables. We use half of the MODIS data (~ 3 million) for training and the remaining half for validation. It takes the trained model less than 10 seconds to computes the CTRC for ~3 million validation datasets. As a comparison, the original algorithm based on the RTM requires more than a half year on a single regular Central Processing Unit.

Figure 4a~c shows the validations of the NN-predicted CTRC variables. The agreements are overall excellent. There is a certain degree of scattering but the number of scattered samples is small (yellowish area). Most cases concentrate near the one-to-one line. The major source of error stems from the discretization of the RTM, which can induce random fluctuations when extracting the ΔF from the profiles of radiative fluxes. This is particularly so for geometrically shallow clouds whose depth is comparable to the model vertical grid size of 50 m. Such randomness may reduce the NN learning accuracy given the deterministic nature of the NN. This can be demonstrated by the better performance of the NN for the LW cloud radiative effect (Fig. 4d), a parameter that is height-independent. The performance is slightly poorer for ΔF_{SW} than ΔF_{LW}, consistent with a more complex radiation physics in the SW. As expected, the NN-predicted global CTRC climatology well agrees with the "truth" one (Fig. S4) despite a slight overestimation of CTRC in the hemispheric winter when the atmosphere is the driest (Fig. S5).

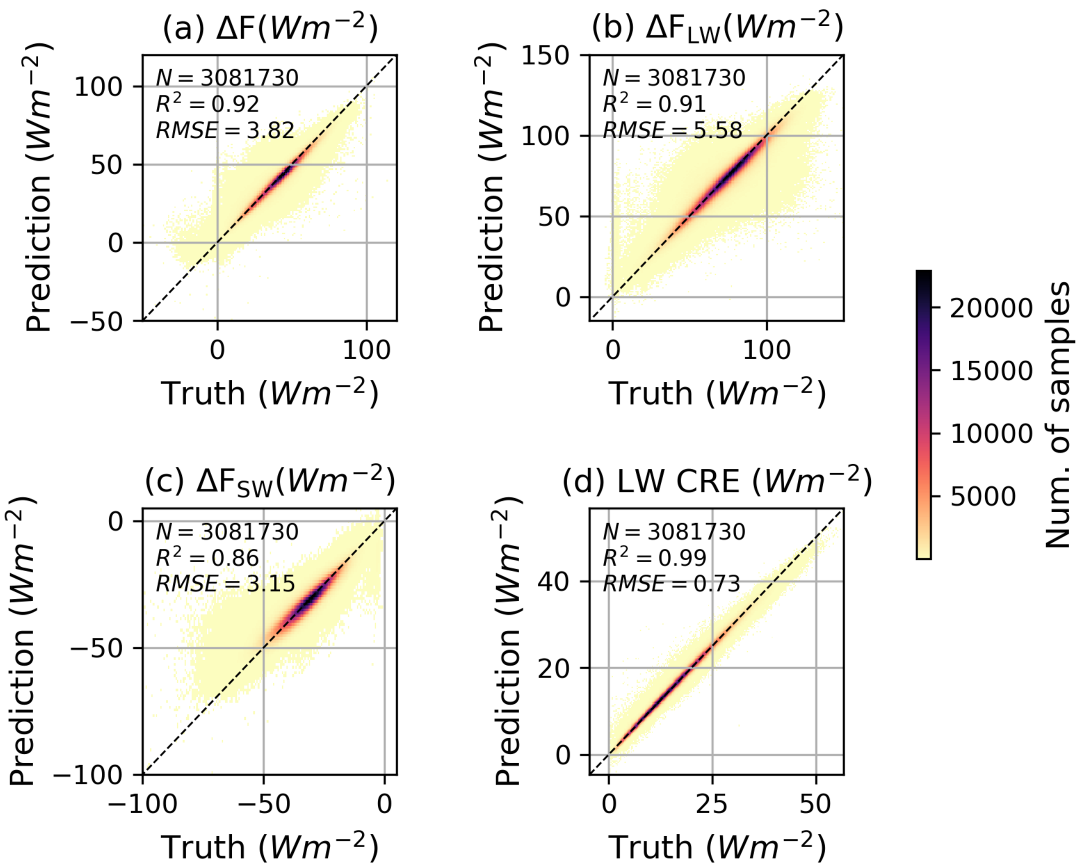

Figure 4: Validation of the neural network prediction against the "truth" from MOIDS retrieval for the instantaneous cloud-top radiative cooling (a), its LW (b) and SW components (c), and the LW cloud radiative effect (d).

6. Conclusion

We generate a one-year climatology of cloud-top radiative cooling (CTRC) and its longwave and shortwave components for global (except poleward of 65 º N/S) marine shallow clouds using a radiative transfer model with inputs of cloud properties from MODIS in combination with reanalysis sounding revised by MODIS-retrieved cloud-top temperature. The CTRC retrieval algorithm was developed in our previous study (Zheng et al., 2019). Analyses of the spatial and temporal distributions of the CTRC yield the following findings:

(1) The global mean cloud-top radiative flux divergence (ΔF) is -61 W m^{-2}, decomposed into the LW cooling of -73 W m^{-2} and SW heating of 11 W m^{-2}. The ΔF is largely a reflection of the LW cooling.
(2) The ΔF has a strong latitudinal dependence with a cooling minimum in the tropics. The cooling increases with the latitude until ~ 30 º N or S. The increase in cooling is primarily driven by the increasing dryness of the free atmosphere that reduces the down-welling LW flux. The cooling peaks in the subtropical eastern ocean under the downward branches of the Hadley circulation. Poleward of 30 º N or S, the cooling decreases slightly, primarily due to the colder atmospheric temperature that weakens the cloud's outgoing thermal emission. If we scale the ΔF by the σT_s^4 to remove the effect by temperature-driven emission, the zonal-mean scaled cooling increases all the way from the tropics to the extra-tropics, a reflection of the decreasing specific humidity of the atmosphere.
(3) There is a hemispheric asymmetry with stronger cooling in the Southern Hemisphere.
(4) The CTRC exhibits distinctive seasonal cycles, with amplitudes of the order 10 to 20 W m^{-2}. The cooling maximizes during the winter when the atmospheric specific humidity is low, which favors the cooling.
(5) The CTRC spatial patterns resemble the marine stratocumulus cloudiness. The resemblance is a result of the fact that environments favoring the formation of stratocumulus decks also favor the strong CTRC.

Finally, we examine the potential of machine learning in speeding up the CTRC retrieval. Trained by the half-year's worth of CTRC datasets with a sample size of ~ 3 million and validated against the other half, the neural network model exhibits a satisfactory performance with the absolute retrieval error of ~6%. The neural network model speeds up the radiative-transfer-model-based retrieval by the order of million times. This will enable generations of much larger CTRC datasets, useful for future more comprehensive research.

Acknowledgments

This study is supported by the Department of Energy (DOE) Atmospheric System Research program (DE-SC0018996).

Data Availability Statement

The MODIS data are from ladsweb.modaps.eosdis.nasa.gov. NCEP reanalysis data are collected from rda.ucar.edu/datasets/ds083.2/. NOAA sea surface temperature data are obtained from https://psl.noaa.gov/data/gridded/data.noaa.oisst.v2.highres.html. The code used to produce the results and the neural network model is available at https://doi.org/10.5281/zenodo.5043713.

Reference:

Austin, P. H., Siems, S., & Wang, Y. (1995). Constraints on droplet growth in radiatively cooled stratocumulus clouds. *Journal of Geophysical Research: Atmospheres, 100*(D7), 14231-14242.

Bony, S., & Dufresne, J. L. (2005). Marine boundary layer clouds at the heart of tropical cloud feedback uncertainties in climate models. *Geophysical Research Letters, 32*(20).

Bretherton, C. S., Blossey, P. N., & Uchida, J. (2007). Cloud droplet sedimentation, entrainment efficiency, and subtropical stratocumulus albedo. *Geophysical Research Letters, 34*(3).

Bretherton, C. S., Uchida, J., & Blossey, P. N. (2010a). Slow manifolds and multiple equilibria in stratocumulus‐capped boundary layers. *Journal of Advances in Modeling Earth Systems, 2*(4).

Bretherton, C. S., Wood, R., George, R., Leon, D., Allen, G., & Zheng, X. (2010b). Southeast Pacific stratocumulus clouds, precipitation and boundary layer structure sampled along 20 S during VOCALS-REx. *Atmospheric Chemistry and Physics, 10*(21), 10639-10654.

Bretherton, C. S., & Wyant, M. C. (1997). Moisture transport, lower-tropospheric stability, and decoupling of cloud-topped boundary layers. *Journal of the Atmospheric Sciences, 54*(1), 148-167.

Caldwell, P., Bretherton, C. S., & Wood, R. (2005). Mixed-layer budget analysis of the diurnal cycle of entrainment in southeast Pacific stratocumulus. *Journal of the Atmospheric Sciences, 62*(10), 3775-3791.

Davies, R., Ridgway, W. L., & Kim, K.-E. (1984). Spectral absorption of solar radiation in cloudy atmospheres: A 20 cm− 1 model. *Journal of Atmospheric Sciences, 41*(13), 2126-2137.

Deardorff, J. (1976). On the entrainment rate of a stratocumulus‐topped mixed layer. *Quarterly Journal of the Royal Meteorological Society, 102*(433), 563-582.

Ghate, V. P., Albrecht, B. A., Miller, M. A., Brewer, A., & Fairall, C. W. (2014). Turbulence and radiation in stratocumulus-topped marine boundary layers: A case study from VOCALS-REx. *Journal of Applied Meteorology and Climatology, 53*(1), 117-135.

Ghate, V. P., Miller, M. A., Albrecht, B. A., & Fairall, C. W. (2015). Thermodynamic and radiative structure of stratocumulus-topped boundary layers. *Journal of the Atmospheric Sciences, 72*(1), 430-451.

Grosvenor, D., & Wood, R. (2014). The effect of solar zenith angle on MODIS cloud optical and microphysical retrievals within marine liquid water clouds. *Atmospheric Chemistry and Physics, 14*(14), 7291-7321.

Guo, Z., Wang, M., Larson, V. E., & Zhou, T. (2019). A cloud top radiative cooling model coupled with CLUBB in the Community Atmosphere Model: Description and simulation of low clouds. *Journal of Advances in Modeling Earth Systems, 11*(4), 979-997.

Haynes, J. M., Haar, T. H. V., L'Ecuyer, T., & Henderson, D. (2013). Radiative heating characteristics of Earth's cloudy atmosphere from vertically resolved active sensors. *Geophysical Research Letters, 40*(3), 624-630.

Henderson, D. S., L'Ecuyer, T., Stephens, G., Partain, P., & Sekiguchi, M. (2013). A multisensor perspective on the radiative impacts of clouds and aerosols. *Journal of Applied Meteorology and Climatology, 52*(4), 853-871.

Huang, Y., Siems, S. T., Manton, M. J., Hande, L. B., & Haynes, J. M. (2012). The structure of low-altitude clouds over the Southern Ocean as seen by CloudSat. *Journal of Climate, 25*(7), 2535-2546.

Kalnay, E., Kanamitsu, M., Kistler, R., Collins, W., Deaven, D., Gandin, L., et al. (1996). The NCEP/NCAR 40-year reanalysis project. *Bulletin of the American Meteorological Society, 77*(3), 437-472.

Kazil, J., Yamaguchi, T., & Feingold, G. (2017). Mesoscale organization, entrainment, and the properties of a closed‐cell stratocumulus cloud. *Journal of Advances in Modeling Earth Systems, 9*(5), 2214-2229.
Klein, S. A., & Hartmann, D. L. (1993). The seasonal cycle of low stratiform clouds. *Journal of Climate, 6*(8), 1587-1606.
Krasnopolsky, V., Fox-Rabinovitz, M., Hou, Y., Lord, S., & Belochitski, A. (2010). Accurate and fast neural network emulations of model radiation for the NCEP coupled climate forecast system: climate simulations and seasonal predictions. *Monthly Weather Review, 138*(5), 1822-1842.
L'Ecuyer, T. S., Wood, N. B., Haladay, T., Stephens, G. L., & Stackhouse Jr, P. W. (2008). Impact of clouds on atmospheric heating based on the R04 CloudSat fluxes and heating rates data set. *Journal of Geophysical Research: Atmospheres, 113*(D8).
Larson, V. E., Schanen, D. P., Wang, M., Ovchinnikov, M., & Ghan, S. (2012). PDF parameterization of boundary layer clouds in models with horizontal grid spacings from 2 to 16 km. *Monthly Weather Review, 140*(1), 285-306.
Li, Z., & Moreau, L. (1996). Alteration of atmospheric solar absorption by clouds: Simulation and observation. *Journal of Applied Meteorology and Climatology, 35*(5), 653-670.
Lilly, D. K. (1968). Models of cloud‐topped mixed layers under a strong inversion. *Quarterly Journal of the Royal Meteorological Society, 94*(401), 292-309.
Muhlbauer, A., McCoy, I. L., & Wood, R. (2014). Climatology of stratocumulus cloud morphologies: microphysical properties and radiative effects. *Atmospheric Chemistry and Physics, 14*(13), 6695-6716.
Nicholls, S. (1984). The dynamics of stratocumulus: Aircraft observations and comparisons with a mixed layer model. *Quarterly Journal of the Royal Meteorological Society, 110*(466), 783-820.
Nicholls, S., & Leighton, J. (1986). An observational study of the structure of stratiform cloud sheets: Part I. Structure. *Quarterly Journal of the Royal Meteorological Society, 112*(472), 431-460.
Pinnick, R., Jennings, S., Chýlek, P., & Auvermann, H. (1979). Verification of a linear relation between IR extinction, absorption and liquid water content of fogs. *Journal of Atmospheric Sciences, 36*(8), 1577-1586.
Platnick, S., King, M. D., Meyer, K. G., Wind, G., Amarasinghe, N., Marchant, B., et al. (2015). MODIS cloud optical properties: User guide for the Collection 6 Level-2 MOD06/MYD06 product and associated Level-3 Datasets. *Version, 1*, 145.
Reynolds, R. W., Smith, T. M., Liu, C., Chelton, D. B., Casey, K. S., & Schlax, M. G. (2007). Daily high-resolution-blended analyses for sea surface temperature. *Journal of Climate, 20*(22), 5473-5496.
Slingo, A., Brown, R., & Wrench, C. (1982). A field study of nocturnal stratocumulus; III. High resolution radiative and microphysical observations. *Quarterly Journal of the Royal Meteorological Society, 108*(455), 145-165.
Stephens, G. (1978). Radiation profiles in extended water clouds. I: Theory. *Journal of the Atmospheric Sciences, 35*(11), 2111-2122.
Stevens, B. (2002). Entrainment in stratocumulus‐topped mixed layers. *Quarterly Journal of the Royal Meteorological Society, 128*(586), 2663-2690.
Stevens, B., Cotton, W. R., Feingold, G., & Moeng, C.-H. (1998). Large-eddy simulations of strongly precipitating, shallow, stratocumulus-topped boundary layers. *Journal of the Atmospheric Sciences, 55*(24), 3616-3638.
Ukkonen, P., Pincus, R., Hogan, R. J., Pagh Nielsen, K., & Kaas, E. (2020). Accelerating radiation computations for dynamical models with targeted machine learning and code optimization. *Journal of Advances in Modeling Earth Systems, 12*(12), e2020MS002226.

Vial, J., Bony, S., Dufresne, J. L., & Roehrig, R. (2016). Coupling between lower‐tropospheric convective mixing and low‐level clouds: Physical mechanisms and dependence on convection scheme. *Journal of Advances in Modeling Earth Systems, 8*(4), 1892-1911.

Wood, R. (2005). Drizzle in stratiform boundary layer clouds. Part I: Vertical and horizontal structure. *Journal of the Atmospheric Sciences, 62*(9), 3011-3033.

Wood, R. (2012). Stratocumulus clouds. *Monthly Weather Review, 140*(8), 2373-2423.

Wood, R., & Bretherton, C. S. (2006). On the relationship between stratiform low cloud cover and lower-tropospheric stability. *Journal of Climate, 19*(24), 6425-6432.

Wyant, M. C., Bretherton, C. S., Rand, H. A., & Stevens, D. E. (1997). Numerical simulations and a conceptual model of the stratocumulus to trade cumulus transition. *Journal of the Atmospheric Sciences, 54*(1), 168-192.

Zheng, Y. (2019). Theoretical understanding of the linear relationship between convective updrafts and cloud-base height for shallow cumulus clouds. Part I: Maritime conditions. *Journal of the Atmospheric Sciences*(2019).

Zheng, Y., Rosenfeld, D., & Li, Z. (2016). Quantifying cloud base updraft speeds of marine stratocumulus from cloud top radiative cooling. *Geophysical Research Letters, 43*(21).

Zheng, Y., Rosenfeld, D., & Li, Z. (2018). The Relationships Between Cloud Top Radiative Cooling Rates, Surface Latent Heat Fluxes, and Cloud‐Base Heights in Marine Stratocumulus. *Journal of Geophysical Research: Atmospheres, 123*(20), 11,678-611,690.

Zheng, Y., Rosenfeld, D., Zhu, Y., & Li, Z. (2019). Satellite‐based estimation of cloud top radiative cooling rate for marine stratocumulus. *Geophysical Research Letters, 46*(8), 4485-4494.

Zhou, X., & Bretherton, C. S. (2019). Simulation of mesoscale cellular convection in marine stratocumulus: 2. Nondrizzling conditions. *Journal of Advances in Modeling Earth Systems, 11*(1), 3-18.

Geophysical Research Letters

Supporting Information for

Climatology of marine shallow-cloud-top radiative cooling

Youtong Zheng[1,2], Yannian Zhu[3], Daniel Rosenfeld[3,4], and Zhanqing Li[1]

Affiliations:
[1]Earth System Science Interdisciplinary Center, University of Maryland, College Park, Maryland, 20742, USA.
[2]GFDL/AOS program, Princeton University, Princeton, New Jersey
[3]Nanjing University, Nanjing, China
[4]Herew University of Jerusalem, Jerusalem, Israel

Contents of this file

1. Text S1~S2
2. Figures S1~S5
3. Table S1

Text S1: Radiative transfer model

The radiative transfer model we use is the Santa Barbara DISORT Atmospheric Radiative Transfer model (Ricchiazzi et al., 1998). We specify the vertical grids with resolutions of 50 m from the surface to 2.25 km and the grid spacing increases with the altitude until the top of the atmosphere, leading to a total of ~ 60 grids in the vertical. The ozone profile and greenhouse gas concentrations are set to default values. The cloud optical depth is uniformly distributed throughout the cloud layer. The wavelength ranges of longwave and shortwave are set as 5 ~ 40 µm and 0.1 ~ 5 µm, respectively. The wavelength inclement is 0.1 µm for shortwave and 0.2 µm for longwave.

Text S2: Configuration of the neural network model

Our NN has a total of four layers. The input and output layers have 25 and 5 nodes respectively, which matches the number of input and output variables. Between them are two fully connected hidden layers with 256 nodes. This adds up to a total of 73733 learnable parameters. We use the Rectified Linear Unit (ReLU) for activation function and the Adam optimizer with a mean squared error loss function. Given the large number of training samples, the specific choices of the hyper-parameters make little difference to the performance. The input data are normalized and shuffled before the training. The total training time was about 7 minutes on a single graphics processing unit.

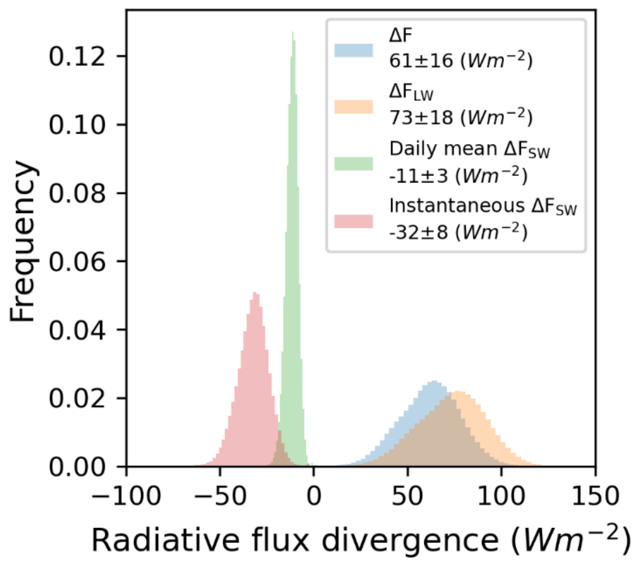

Figure S1: Probability density functions of cloud-top radiative flux divergences.

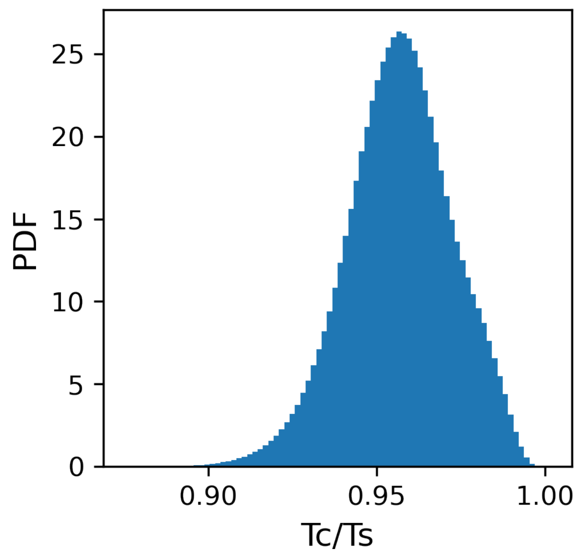

Figure S2: Probability density functions of the ratio between cloud-top temperature and sea surface temperature.

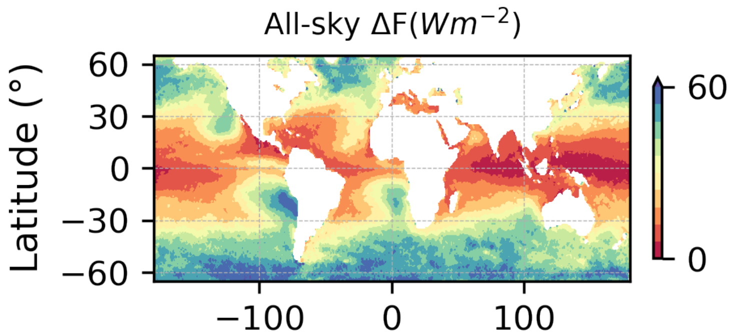

Figure S3: Annual-mean all-sky cloud-top radiative cooling.

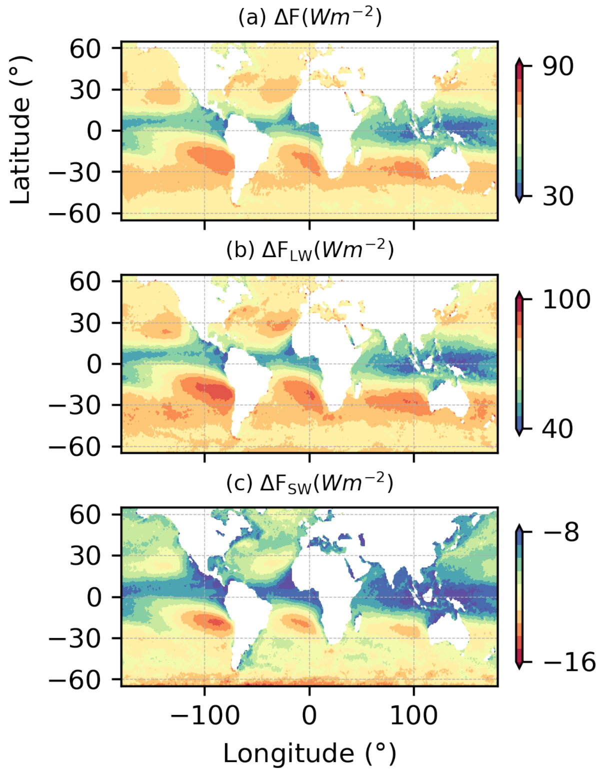

Figure S4: Neural-network-estimated global distribution of annually-averaged cloud-top radiative cooling (a), its LW (b) and SW components (c).

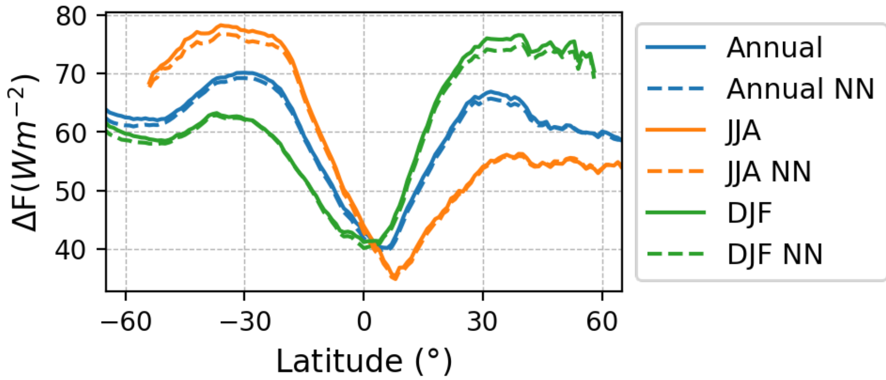

Figure S5: Zonal-mean meridional variations of cloud-top radiative cooling computed from the radiative transfer model (solid) and the neural network (dashed) for boreal summer (orange) and winter (green).

Input variables	Unit	Output variables	Unit
Cloud optical depth	Unitless	**Cloud top radiative cooling, ΔF**	W m^{-2}
Cloud droplet effective radius	μm	**Cloud top longwave cooling, ΔF_{LW}**	W m^{-2}
Cloud top temperature	K	**Cloud top shortwave heating, ΔF_{SW}**	W m^{-2}
Solar zenith angle	degree	Cloud base longwave heating	W m^{-2}
Sea surface temperature	K	Cloud longwave radiative effect	W m^{-2}
Absolute temperature from 1000 hPa to 100 hPa with 100 hPa interval	K		
Relative humidity from 1000 hPa to 100 hPa with 100 hPa interval	%		

Table 1: Input and output variables for the Neural Network. The CTRC variables used in this study are highlighted in bold.

Reference

Ricchiazzi, P., Yang, S., Gautier, C., & Sowle, D. (1998). SBDART: A research and teaching software tool for plane-parallel radiative transfer in the Earth's atmosphere. *Bulletin of the American Meteorological Society, 79*(10), 2101-2114.